Experimental and computational study of complex shockwave dynamics in laser ablation plumes in argon atmosphere

S. S. Harilal, G. V. Miloshevsky, P. K. Diwakar, N. L. LaHaye, and A. Hassanein
Center for Materials under Extreme Environment, and School of Nuclear Engineering, Purdue University, West Lafayette, Indiana 47907, USA

(Received 5 July 2012; accepted 30 July 2012; published online 10 August 2012)

We investigated spatio-temporal evolution of ns laser ablation plumes at atmospheric pressure, a favored condition for laser-induced breakdown spectroscopy and laser-ablation inductively coupled plasma mass-spectrometry. The 1064 nm, 6 ns pulses from a Nd:YAG laser were focused on to an Al target and the generated plasma was allowed to expand in 1 atm Ar. The hydrodynamic expansion features were studied using focused shadowgraphy and gated 2 ns self-emission visible imaging. Shadowgram images showed material ejection and generation of shock fronts. A secondary shock is observed behind the primary shock during the time window of 100-500 ns with instabilities near the laser cone angle. By comparing the self-emission images obtained using fast photography, it is concluded that the secondary shocks observed in the shadowgraphy were generated by fast moving target material. The plume front estimates using fast photography exhibited reasonable agreement with data obtained from shadowgraphy at early times $\leq$400 ns. However, at later times, fast photography images showed plume confinement while the shadowgraphic images showed propagation of the plume front even at greater times. The structure and dynamics of the plume obtained from optical diagnostic tools were compared to numerical simulations. We have shown that the main features of plume expansion in ambient Ar observed in the experiments can be reproduced using a continuum hydrodynamics model which provided valuable insight into the expansion dynamics and shock structure of the plasma plume. © *2012 American Institute of Physics*. [http://dx.doi.org/10.1063/1.4745867]

I. INTRODUCTION

Laser ablation (LA) and plasma generation already have numerous applications. These include narrowband short wavelength light sources for lithography[1] and microscopy,[2] broadband sources for spectroscopy,[3] analytical applications ranging from laser-induced breakdown spectroscopy (LIBS),[4] LA inductively coupled plasma mass-spectrometry (LA-ICP-MS)[5] to matrix-assisted laser desorption/ionization (MALDI),[6] micromachining,[7] pulsed laser deposition (PLD),[8] nanoparticle production,[9] laser ion source (LIS),[10] etc. In light source applications, pulsed, high intensity lasers are used to heat and vaporize the material of interest in vacuum.[11] In that scenario, the plasma formed by the leading edge of the laser pulse will be heated efficiently by the rest of the laser pulse. This is true when the duration of the laser pulse (τ_p) is greater than 100's of ps. For short pulse laser ablation, with $\tau_p \leq 1$ps, the plasma formation takes place after deposition of the entire laser pulse energy onto the target. For nanosecond "long pulse" laser ablation, according to Singh and Narayan,[12] the plasma expands isothermally during the laser pulse followed by adiabatic expansion after the laser pulse termination. During the isothermal expansion regime, initially the laser interacts with the target and when the initial low density, low temperature plasma plume is formed, collisional ionization and excitation, coupled with the remainder of the laser pulse energy rapidly heats and ionizes the plasma.[13] During adiabatic expansion regime, the plasma expands freely into vacuum. The entire process of nanosecond laser ablation, plasma formation, and expansion has been studied extensively by various groups using various plasma diagnostic tools and has been extensively modeled.[12,14–20]

Some applications of laser-produced plasmas (LPPs) are in the presence of moderate ambient gas (1-10^3 mTorr). For example, in PLD, an ambient gas is always used as a moderator for energetic particles. The laser passage through an ambient gas dramatically affects the laser-target, laser-plasma generation, and plasma expansion features. The addition of an ambient gas during plasma expansion will initiate several complex processes.[21–23] In fact, the presence of ambient gas influences the entire processes of plasma generation as well as expansion. Instead of free expansion in vacuum, the plume expansion in the presence of a moderate ambient gas leads to internal plume structures, plume splitting, sharpening, confinement, etc. Previous experimental studies have shown that the expansion features of the plume heavily depended both on laser properties, atomic mass and pressure of the ambient gas, and focusing conditions.[24,25] Most of the analytical applications of laser-plasma take place at atmospheric pressure or under a flowing gas medium. For example, typically LIBS is performed at atmospheric air pressure[26] while LA-ICP-MS is carried out in the presence of a flowing gas[5] (typically Ar or He). In both conditions, initially the plume pressure will be significantly higher than the ambient pressure and will compress the ambient gas atoms leading to a formation of shock front and at later stages, plume expansion ceases when its pressure equilibrates with the background pressure.

Numerous theoretical approaches such as analytical methods, fluid dynamic models, and Monte Carlo methods are used for describing the expansion of plasma plume and understanding its temporal and spatial evolution.[27] Many theoretical studies have considered plasma expansion in vacuum or at a very low-pressure background.[28–30] In this case, in agreement with experiments, the expansion involves plume formation and free-plume expansion in vacuum.[31,32] The plasma expansion into 1-atm background gas was also intensively studied by several research groups.[14–18,33] It is found that the interaction of the expanding plume with a high-pressure background gas crucially affects the expansion dynamics. The expansion is spatially confined and strongly decelerated with the formation of shock waves and stopping. The dimensions of the plasma plume are much smaller compared to that observed during the expansion in vacuum. The propagation of shock waves in a background gas has been quantitatively predicted using the analytical "blast wave" model.[34,35] The internal shock-wave-like structure with shock waves traveling between the front and the center of the expanding plume has been reported in a number of studies.[31,33,36] The initial state of vortex formation due to plasma plume ambient gas interactions has been also observed.[37] Even though LPP expansion in the presence of an ambient gas has been a topic of interest over the last several decades and many efforts have been made, the physics behind the entire process has not been fully understood, essentially due to the complexity of the various physical processes involved.

In this paper, we report on the expansion dynamics as well as internal plume structure of laser ablated aluminum plasma in Ar at atmospheric pressure using time resolved focused shadowgraphy and gated 2-dimensional imaging. We have also performed computational fluid dynamics (CFD) simulations that support and further clarify the behavior observed in the experimental data.

II. EXPERIMENTAL AND MODELING DETAILS

For producing plasmas, 1064 nm, 6 ns (full width at half maximum (FWHM)) pulses from an Nd:YAG laser was used. The target was placed in a stainless steel vacuum chamber which was filled with Ar at 1 atmospheric pressure. The laser beam was focused, at normal incidence, onto the target using a plano-convex lens with an estimated spot diameter of 500 μm. A 2-mm thick aluminum piece in the form of a slab was used as the target. We used focused shadowgraphy set up for recording shadowgrams. In this set up, a relay lens is used to image the plasma plume onto a CMOS CCD detector. A frequency doubled Nd:YAG laser with wavelength 532 nm and pulse duration of 8 ns was used as a probe light. The incoming probe laser beam constituted the light source for the formation of each shadowgram. The probe laser was synchronized with the plasma generating laser using a delay generator with a maximum temporal jitter of $\pm$1 ns. A synchronized CCD camera captured the resulting shadowgram of the laser produced plasma. The delay between pump and probe lasers and the camera is varied to interrogate the plasma plume at different times during its expansion. A narrow band-pass filter with a peak transmission wavelength of 532 nm rejected broadband optical emission from the plasma reaching the detector. Fast photography was accomplished with an intensified CCD (ICCD) camera placed orthogonal to the laser beam. An objective lens (Nikon Macrolens, $f = 70$-200 mm) was used to image the plume region onto the camera to form a two-dimensional image of the plume intensity. The visible radiation from the plasma was recorded integrally over the wavelength range of 350–900 nm.

The modeling of the expansion of LPP plume in the presence of 1 atm Ar gas is carried out using the rhoCentralFoam solver,[38] a part of the open source OpenFOAM toolbox.[39] It is a density-based solver for viscous compressible flows using the conservative formulation. The central upwind schemes[40] are implemented to accurately resolve shocks and contact discontinuities in compressible subsonic and supersonic flows. The solver uses the Riemann-free approach, which does not require the characteristic decomposition and Jacobian evaluation, making it computationally inexpensive. The governing equations of compressible fluid motion are solved in an Eulerian frame using the finite volume method.[41] The set of equations can be written as[38]

$$\frac{\partial \rho}{\partial t} + \nabla \cdot (\rho \vec{u}) = 0, \tag{1}$$

$$\frac{\partial \rho \vec{u}}{\partial t} + \nabla \cdot [\vec{u}(\rho \vec{u})] = -\nabla p - \nabla \cdot \bar{\bar{\tau}}, \tag{2}$$

$$\frac{\partial \rho E}{\partial t} + \nabla \cdot [\vec{u}(\rho E)] = -\nabla \cdot [\vec{u} p] - \nabla \cdot [\vec{u} \cdot \bar{\bar{\tau}}] - \nabla \cdot \vec{q}. \tag{3}$$

Equation (1) describes the continuity of mass, Eq. (2) is the Navier-Stokes equation, and Eq. (3) is the conservation of energy. Here ρ is the mass density, $\vec{u}$ is the fluid velocity, p is the pressure, $E = e + \vec{u}^2/2$ is the total specific energy with e is the specific internal energy, $\bar{\bar{\tau}}$ is the viscous stress tenser, and $\vec{q} = -k\nabla T$ is the heat flux where T is the temperature and k is the conductivity. The perfect gas equation of state $p = \rho RT$ and $e = (\gamma - 1)RT$ is used to close Eqs. (1)–(3). Here, R is the gas constant and $\gamma = c_p/c_v$ is the ratio of specific heats at constant pressure and volume. The sequential operator-splitting approach[38] is used to solve the momentum and energy equations. First, the inviscid equations (1) and (2) are solved explicitly for the convective terms. Second, the momentum and heat diffusion terms are then included as implicit corrections to the inviscid solution. An implicit Euler scheme is used for time derivatives. The computational domain in a 2-dimensional Cartesian frame is used with x and y lengths of 5 mm. The domain representation can be seen in Sec. III C. A grid spacing of 10 μm (500 $\times$ 500 cells) is imposed. The domain is filled with Ar gas at a temperature $\sim$300 K, pressure $\sim$1 bar, and a mass density $\sim$1.78 kg/m^3. The plasma plume is assumed to be formed within the laser spot with a radius of $\sim$250 μm and a depth of $\sim$100 μm at the center of the spot that corresponds to a reported depth measurement under similar irradiance conditions used in the present experiment.[42] The cross-sectional *shape of the crater* is assumed to be oval with an *arc* connecting a point on the

peripheral edge of the laser spot with that in the center of spot at a depth ~100 μm. The plasma and background Ar are treated as a compressible ideal gas. The computations are carried out for three plasma temperatures ~5, ~10, and ~15 eV. In all three cases, the initial internal pressure of plasma is assumed constant, ~210 MPa. Under these conditions, the corresponding mass density of plasma calculated from the ideal gas law is ~11.8, ~5.9, and ~3.9 kg/m^3. Both the plasma plume and background gas are motionless at time $t = 0$. The plasma is then allowed to expand under its own pressure.

III. RESULTS AND DISCUSSION

A. Focused shadowgraphy

Shadowgraphy is a well-known diagnostic tool for monitoring the spatial variation of refractive index across a probe beam.[43] The shadowgram corresponds to second order of the refractive field which will reveal the inhomogeneities in the medium of interest in the best possible way. Two commonly used shadowgraphic methods are direct shadowgraphy and focused shadowgraphy. In direct shadowgraphy, a diverging or parallel beam is used to monitor the refractive changes in the medium. In focused shadowgraphy, a relay lens is used to image the refractive medium onto the detector. The main advantage of focused shadowgraphy is that it allows variable magnification of the shadowgram. We employed the focused shadowgraphy experimental method for investigating the dynamics of expanding laser plumes at atmospheric pressure.

Laser ablation in the presence of ambient gas forms classical Taylor-Sedov blast waves when the interaction between the plasma and the ambient gas is collisional and when the mass of the swept ambient gas is greater than the mass of the ablated plasma.[35] Fig. 1 gives a series of shadowgram images illustrating the spatial and temporal evolution of the ablation process and plume expansion into the ambient Ar. The laser energy used in the experiment was 100 mJ with a focal spot diameter of 500 μm. The time given in the figure corresponds to a time index after the peak of the plasma generating laser. Shock fronts can easily be seen in the shadowgrams along with ejected material and an altered second feature is observed inside the plume-background compressed region especially at times 100–500 ns. The refractive index change caused by the plasma is evident even during the plasma generating laser-pulse. Although the boundary of discontinuity in refractive index is very evident at all frames, the shadow images recorded at the earlier times ($\leq$50 ns) showed darkened regions without any structures. This could be due to high densities at early times of plasma radiation and/or spatial mixing caused by the long probe laser pulse width. It should be noted that the probe laser beam will become opaque when the plasma density reaches critical density. Even if the plasma density is lower than the critical density of the probe beam, at high plasma densities the free-free absorption can attenuate the probe beam. Apart from that the pulse width of the probe beam used in the present experiment is 8 ns which relatively long considering the fast expansion of the plume in the initial times which leads to spatial mixing that cannot be avoided.

A distorted structure on the tip of the external shockwave is visible from very early time histories during plasma formation which could be due to the formation of a laser supported detonation (LSD) wave as has been shown in earlier studies.[44] Russo *et al.*[45] observed LSD in Ar and its propagation at ~10 ns after the laser pulse for energies of 10 and 30 mJ. LSD formation is more evident in the case of argon due to its low ionization potential (15.759 eV) and higher density of argon. Because of the low ionization potential of Ar, the compressed gas layer behind the external shockwave is highly ionized and can absorb the incoming laser pulse and can generate a sustaining LSD wave during the laser pulse duration. LSD creates a region of high electron temperature and electron density which results in non-uniform heating of the adjacent shockwave and vapor plume.[45] The LSD wave stops propagating by the end of laser pulse but due to non-uniform heating, the central tip of the vapor plume and adjacent shockwave continues to move faster than rest of the plume and results in formation of irregular structures on the top of the external shockwave as seen in the shadowgram images. This feature disappears after about 80 ns.

For time histories >50 ns, the compressed region or shock front is very evident in all the images. The shock front is seen to be uniform and approximately spherical to the target normal direction. The secondary shock observed behind the primary shock wave is also spherical though the part of the wave near to the laser cone angle showed instabilities. Fig. 2 shows a shadowgram recorded at 150 ns along with intensity changes in the shadowgram in a direction perpendicular to the

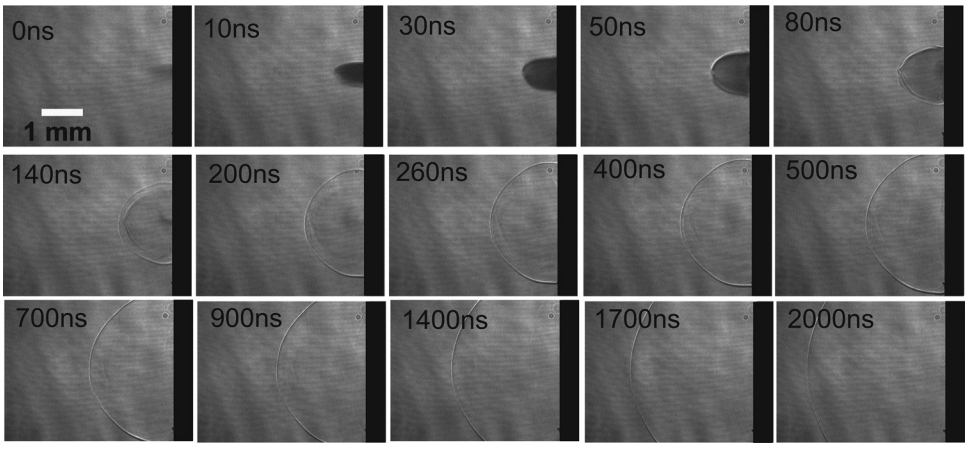

FIG. 1. Shadowgrams taken at different times during the evolution of the plasma plume. The times given in the figure corresponds to the times after the peak of the plasma generating laser pulse.

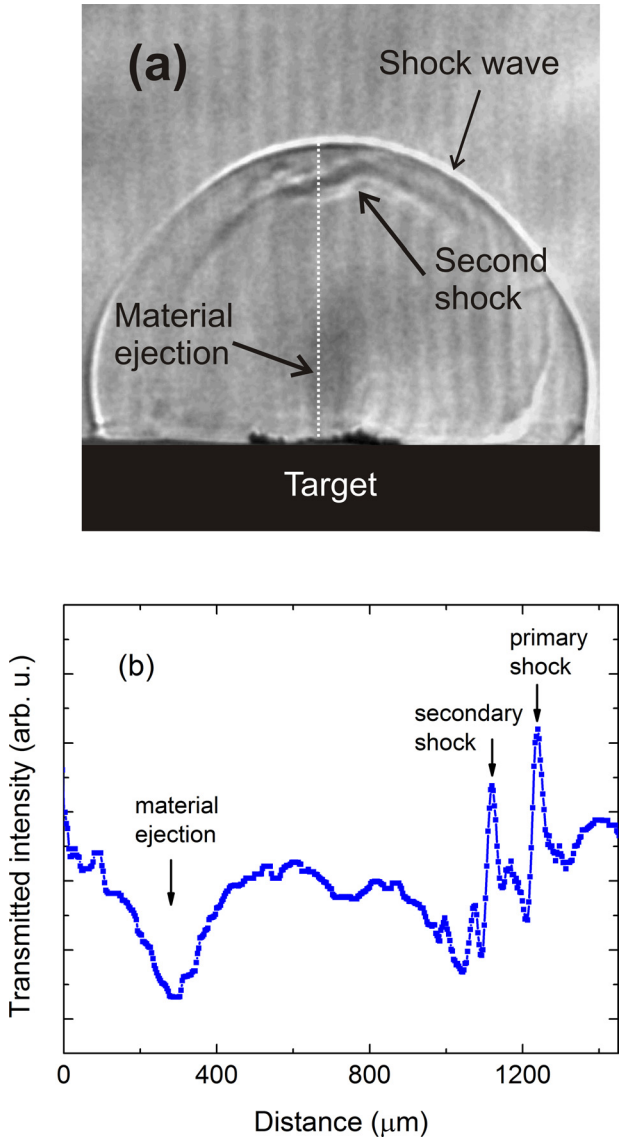

FIG. 2. (a) Typical shadowgram image recorded during the laser ablation of Al at 1 atm Ar pressure at 150 ns. The structures noticed are marked. (b) The intensity change in the shadowgram along the target normal is given. The intensity change is obtained slightly away from the beam central position (represented by the dotted line in (a)) to avoid the deformation noticed in the secondary shock.

target. The primary shock wave and the secondary shock wave are marked in the figure. The secondary shock wave is visibly thicker than the primary shock wave. In the collisional shock, the thickness of the shock front is of the order of collisional mean free path of the particle in the shock front. Decreasing pressure leads to increased particle mean free path leading to the formation of thicker shock front. The intensity contour plots obtained from the shadowgram given in Fig. 2 clearly shows multiple density jumps. However, these features are apparently absent at later times of plasma evolution. Callies *et al.*[46] observed similar structure inside the plume and noticed the second discontinuity corresponds to plasma luminescence. At later stages of expansion, the secondary shock could be a part of an internal shock-wave structure within the plasma plume described by Brode.[19] For nanosecond laser plasma generation for the laser intensities reported here, a portion of the laser pulse at the rising edge ablates and heats a thin nm layer of target material.[47] Free electrons, which are accelerated by the lasers electric field, drive collisional excitation and further ionization. The coupling of the laser pulse to the target mass (for ablation) or to the plasma plume depends strongly upon the local plasma frequency, f_p and hence electron density, N_e ($f_p \approx 8.9 \times N_e^{1/2}$). In actuality, the laser pulse will shift between target ablation and plume heating many times during the laser pulse. The fast moving plume species push forward the gas pile up (primary shock wave). As time evolves, the velocities of target atoms dissipated by nearby gas atoms leading to reduction in velocity. But for the primary shock wave, the density peak still exists and keeps moving due to energy obtained from the target atoms. The evolution of the shock front given in Fig. 2 shows a wider density distribution for the secondary shock wave compared to the primary shockwave which clarify our claims.

The inner structure noticed in the back of the primary shock front contains an instability region near to the laser cone. Grun *et al.*[48] observed instabilities in Taylor-Sedov blast waves propagating through a uniform gas with low adiabatic index (γ). They observed a stable blast wave in the presence of nitrogen gas ($\gamma_N = 1.3$) while the entire blast wave geometry showed instabilities in the presence of Xe gas ($\gamma_{Xe} = 1.06$). However, in the present experiment, the instabilities are noticed in the secondary shock waves and that only occurred near to the target normal direction (laser cone angle). Since the deformity of the inner spherical front appears only at the laser cone angle, we believe that this refractive index modulation is caused by laser-plasma interaction. In fact a, deformation in the plume-background interface is noticeable at the plume front position even at earlier times (see Fig. 1), though internal structure details are not apparent due to significant probe beam absorption by the plasma/spatial mixing. As time evolves, internal features are more evident and the internal spherical front detached from the shock front and moves slowly.

As the shock front moves away from the target surface, it accrues mass resulting in deceleration. The position-time (R-t) plot obtained from the shadowgram is given in Fig. 3.

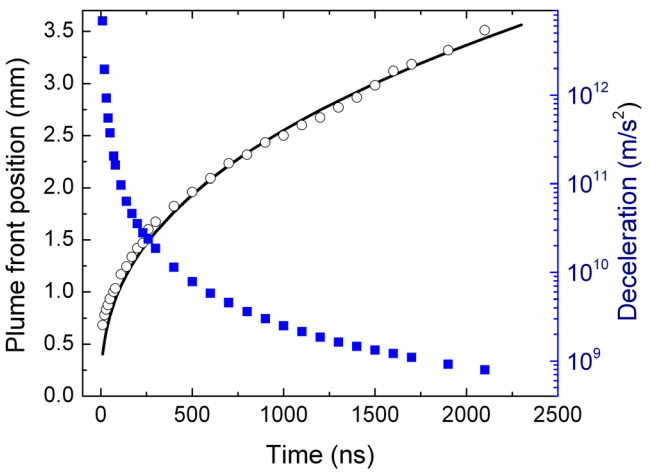

FIG. 3. Position-time plots obtained from shadowgraphic images are given (hollow circles). The solid line fit corresponds to blast wave model. The deceleration of the plume expansion estimated from R-t curve is shown in the right curve (solid squares).

The data show the plume expands very rapidly in the first few 10's of nanoseconds. However, the velocity of the plume is found to decrease rapidly with time. Typically, these plasmas expand freely in vacuum[49] with a velocity ~100 km/s indicating that the ambient gas starts to slow the plasma expansion even at the earliest times of its generation. The estimated plume deceleration is also given in Fig. 3 shows the influence of 1 atm ambient gas on expansion dynamics of the plasma plume. The recorded shadowgrams show that the plume expansion approximately follows spherical expansion. We compared the R-t data with Taylor-Sedov theory which state that blast wave propagation from a point explosion follows the following expression:[35]

$$R = \xi \left(\frac{E}{\rho}\right)^{1/n+2} t^{2/n+2}, \tag{4}$$

where t is the delay time following ignition, ρ_b is the background gas density, E is the amount of energy released during the explosion, and ξ is a constant which is depended on the specific heat capacity ratio. In general, Eq. (4) can be rewritten as $R = at^b$. The blast wave model described in Eq. (4) can be used to characterize laser plasma plume expansion dynamics in the presence of an ambient atmosphere. The value of b which is 2/n + 2, where n = 3, 2, or 1 for spherical, cylindrical or plane wave shock wave propagation respectively. Hence for the spherical blast wave, Eq. (4) follows $R = at^{0.4}$ and respective fittings are given in Fig. 3 (solid black line) which shows good agreement with recorded plasma expansion behavior especially at times >300 ns. The shadowgrams can also be used for estimating the shock wave pressure[35] by using the following equation:

$$p_{sw} = 2\left(\frac{2\xi}{5}\right)^2 \left(\frac{E^2\rho_b^3}{t^6}\right)^{0.2}. \tag{5}$$

The calculated pressures of the shock wave at different times after laser ablation are shown in Fig. 4. The maximum recorded pressure at 60 ns after the peak of the laser pulse is ~100 MPa and its value decreases with the shock wave expansion. The estimated shock pressure at 2 μs is ~1 MPa which is an order of magnitude higher than the pressure of the ambient gas (0.1 MPa).

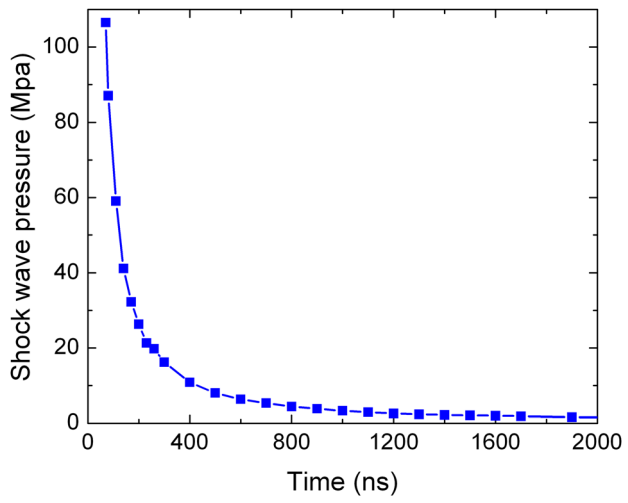

FIG. 4. Shock wave pressure estimated using Eq. (5).

B. Fast photography of the plume

Fast photography that provides two-dimensional snap shots of the three-dimensional LPP propagation is one of the versatile diagnostic tools for understanding the expansion dynamics of laser created plumes especially when the plume interacts with an ambient gas.[25] This capability becomes essential for the hydrodynamic understanding of plume propagation and reactive scattering.[50] Typically, emission from the plasma begins soon after the laser photons reach the surface. The ICCD images of the expanding plume recorded at different times after the onset of plasma are given in Fig. 5. The gate time of the intensifier on the ICCD was kept to 2 ns for all images. All images shown here have been normalized to the peak intensity in that image for clarity. The imaging was performed perpendicular to the target normal and hence the images given in Fig. 5 represent a side view of the expanding plume.

The 3-dimensional plume propagation is governed by the initial pressure gradients and shape of the plume at the end of the laser pulse. Previous studies using ICCD fast photography showed that[32] as the pressure increases from vacuum, there exist a transition regime, where the plume is characterized by strong interpenetration of the plasma species and background gas that leads to plume splitting and sharpening. During this stage of mutual penetration of laser plasma and ambient gas, a considerable fraction of the kinetic energy is converted into heat which in turn increases the temperature of the gas and radiation. The pressure range of the transition regime depends on several experimental parameters including, target and ambient gas masses and laser intensity. However, such features are found to be absent at gas pressures ≤0.1 Torr Ar atmosphere. At one atmospheric pressure, the plume emission appears both uniform and homogeneous without many internal structures as well as sharp boundary separating the plume and ambient gas medium (as seen in Fig. 5). It should be noted that the presence of a background gas during LPP expansion can lead to formation of stationary ambient plasma.[22] This is caused by ionization of ambient gas atoms by prompt electrons and/or intense extreme ultraviolet light coming out from the early stages of plasma formation. So unlike shadowgraphy, a sharp boundary is not expected when self-emission is used to monitor the plume-background interface. The expansion behavior of the plasma at 1 atm is distinctly different from plasma expansion in moderate ambient pressures (10-500 mTorr), where a sharp emitting boundary zone is seen separating the plume and ambient gas.[32] This shock boundary is found to be absent when the plume expansion takes place at 1 atm.

The time sequence of ICCD images shows that the plume expands rapidly in the first 100 ns and then propagates slowly. Shadowgraphic results showed the ambient gas decelerate the plasma even at the initial times of plasma generation. Even with 2 ns gating, the intensity features in the plume images do not show internal structures at times

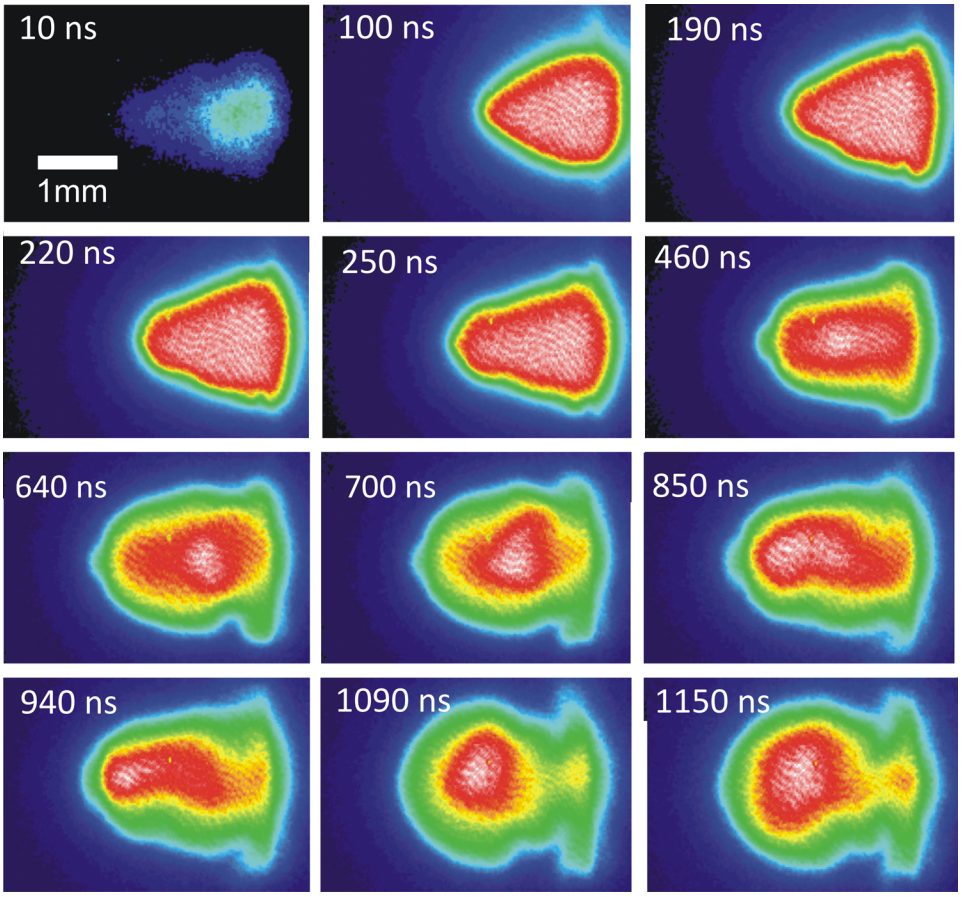

FIG. 5. ICCD images of laser ablated plumes at 1 atm Ar pressure.

≤250 ns. However, such internal structures are evident at later times. Emission intensity as a function of distance along the direction of plume expansion is given in Fig. 6 at different times after the evolution of the plume. These plots are obtained from the ICCD images and provide useful insight into the internal structures in the plume. For easier comparison, each profile has been normalized to its maximum intensity. The distance zero corresponds to target position. Low intensity radiation observed at negative distances is due to reflection of the light from the target sample surface and captured by the ICCD.

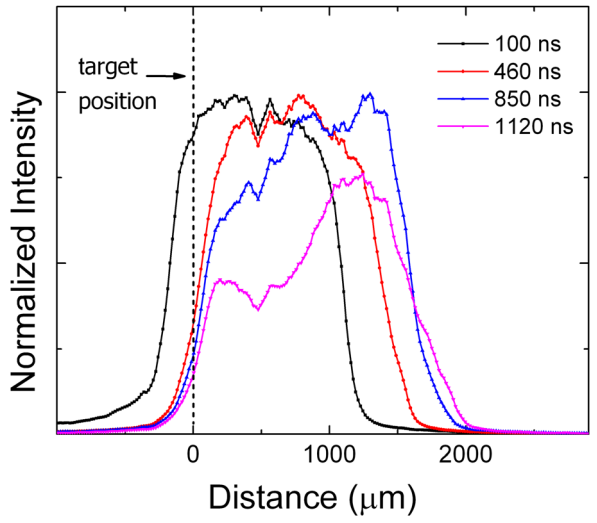

FIG. 6. Intensity counts (scale units) obtained from the ICCD images along the plume normal expansion direction are given for various times during the evolution of the plasma. For better comparison, all the intensity profiles are normalized with respect to their maximum intensity. The distance zero corresponds to target position.

The emission intensity profiles show a single peak distribution at 100 ns after the onset of plasma formation indicating uniform bulk emission along the target normal. Even though the plume propagation is noticeable at the intensity distribution recorded at 460 ns, the self-emission from the plume is found to be uniform. However, at later times, a clear indication of center of mass shift away from the target is evident and the intensity is found to peak at the plume-ambient boundary.[51]

Similar to shadowgraphy images, ICCD images were used to generate distance-time (R-t) plots and the results obtained, together with the shadowgraphy results are given in Fig. 7. The shock front boundary is found to be very well defined in shadowgraphy images while the self- emission recorded using the ICCD showed significant uncertainty in recording plume front positions. In the present case we took the plume front position based on a 90% reduction in the maximum intensity. The data obtained from shadowgraphy plume front positions and Taylor-Sedov shock fit are also given in Fig. 7 for better comparison. The data sets showed reasonable agreement with data obtained from shadowgraphy and ICCD plume imaging at early times (times ≤ 400 ns). However, after ∼400 ns, there exists a discrepancy in plume front positions obtained from the two diagnostic methods. The plume propagation data obtained from ICCD imaging are found to be confined with little or no movement,

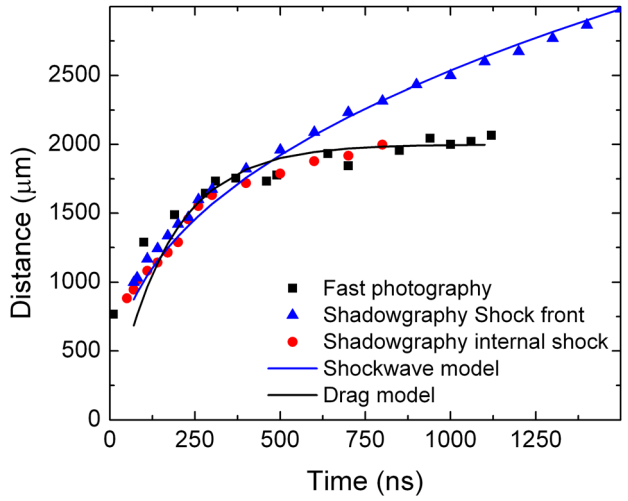

FIG. 7. Distance-time (R-t) plot obtained from the ICCD images are given along with data obtained from shadowgraphy images. The points correspond to experimentally taken data and the smooth curves represent the various modeling fits. The ambient-plume interface obtained from the shadowgram closely follows a Taylor-Sedov shock fit while the ICCD plume front positions as well as the inner shock front obtained from shadowgrams agree well with a drag force model fit especially at later times.

while the shadowgraphic images showed propagation of the plume front even at larger times.

The self-emission from the plasma is found to cease at later times while the plume-ambient interface is continuously propagating at larger distances away from the target. This implies the major emission from the plasma is due to target bulk atoms/ions while the plume-ambient boundary is not generating any visible emission except the refractive changes in the medium. In the shadowgraphy images, we noticed an internal shock wave appeared in the earliest times of plume propagation. We plotted R-t data obtained from the internal shock wave shown in Fig. 7 which is found to be in reasonable agreement with data obtained from ICCD images. This clearly highlights the internal shock noticed in the shadowgraphy is generated by target bulk atoms.

The shock model fit is found to be good only for shadowgraphy plume-ambient gas interface zone and the plume propagation obtained from ICCD images at early times. Previous studies showed that the drag model provides a better fit at later phases of plume expansion in a highly viscous background medium, which is given by[32]

$$R = R_o[1 - \exp(-\beta t)], \tag{6}$$

where R_0 is the stopping distance of the plume and β is the slowing coefficient ($R_0\beta = v_0$). The drag model predicts that the plume will eventually come to rest due to resistance from collisions with the background gas. The drag model fit given in Fig. 7 agrees well with plume propagation data obtained from ICCD images as well as the secondary inner shock observed in the shadowgraphy images.

C. Modeling results

The hydrodynamic equations (1)–(3) for non-steady state expansion of plasma plume are numerically solved. The spatial and temporal evolution of pressure, density, temperature and velocity are calculated. Here, the results are presented for the case of plasma expansion with an initial temperature of ~5 eV and mass density of ~11.8 kg/m^3. The initial plasma temperature and density assumption is based on reported plasma parameters under similar irradiation conditions.[49,52,53] The profiles of pressure, temperature, mass density, and the y-component of velocity (velocity along the target normal direction) are shown in Fig. 8 for different times. It is evident that strong shock waves are produced as the plume expands into the background argon atmosphere (Fig. 8(a)). The plume pressure drops rapidly during first tens of nanoseconds in agreement with the experimental data (Fig. 4). Complex motion of plasma arises behind the developed shock wave. At $t \sim 100$ ns, the pressure inside the expanding plume becomes lower than that at the plasma-argon interface. At $t \sim 400$ ns, in the region near $y = 0$ the pressure reaches the value of ~0.04 MPa which is lower than the background pressure, ~0.1 MPa. At ~1000 ns, a sharp increase in pressure is noticed near the plume's center. The plume enters into an oscillating stage of its expansion at $t \geq 1400$ ns (at least 3–4 internal shock waves are seen in Fig. 8(a)). The internal shock waves travels several times between the plume's center and front. At later times ($t > 1000$ ns), the plume front moves more slowly due to the confining effect of the argon background. However, the sharp interface between plume and background is retained even at times $t \sim 2000$ ns. The pressure at the shock front is ~1 MPa that is in remarkably good agreement with an experimental estimate (Fig. 4).

At early times $t \leq 400$ ns, the dynamics of the plume's temperature (Fig. 8(b)) is broadly similar in profile to the plumes pressure profile. However, at $t \sim 400$ ns, the temperature is ~2000 K near $y = 0$ which is considerably higher than the simulated background temperature, ~300 K. At later times ($t \geq 1000$ ns), the temperature is in the region of 5000 K, which is effectively the plume's flow temperature and is related to the initial momentum of the plasma species during the initial explosive expansion. The mass density of plume quickly decreases from ~11.8 kg/m^3 to the background density ~1.7 kg/m^3 during $t <$ ~400 ns (Fig. 8(c)). The mass swept by the shock front of the plume then forms a thin shock layer which travels with the shock wave leaving behind it a low-density region. The inner plume mass density is lower by approximately an order of magnitude compared to the argon background density.

The *y*-component of velocity increases sharply from zero to ~4 km/s at time $t \sim 40$ ns (Fig. 8(d)). This value is even higher at shorter times (not shown) which also corresponds to initial plasma temperatures. The velocity of the shock wave decreases significantly at $t \sim 400$ ns. It is seen that at $t >$ ~400 ns an internal shock wave is formed near the plume's center traveling in the same direction as the primary one. At $t >$ ~1400 ns, the plasma flow is reversed toward the plume's center behind the internal shock. At this stage, the motion of plasma in the plume near the surface of the target is very complicated due to the development of a ring-like vortex, sucking denser Ar back towards the target (not shown).

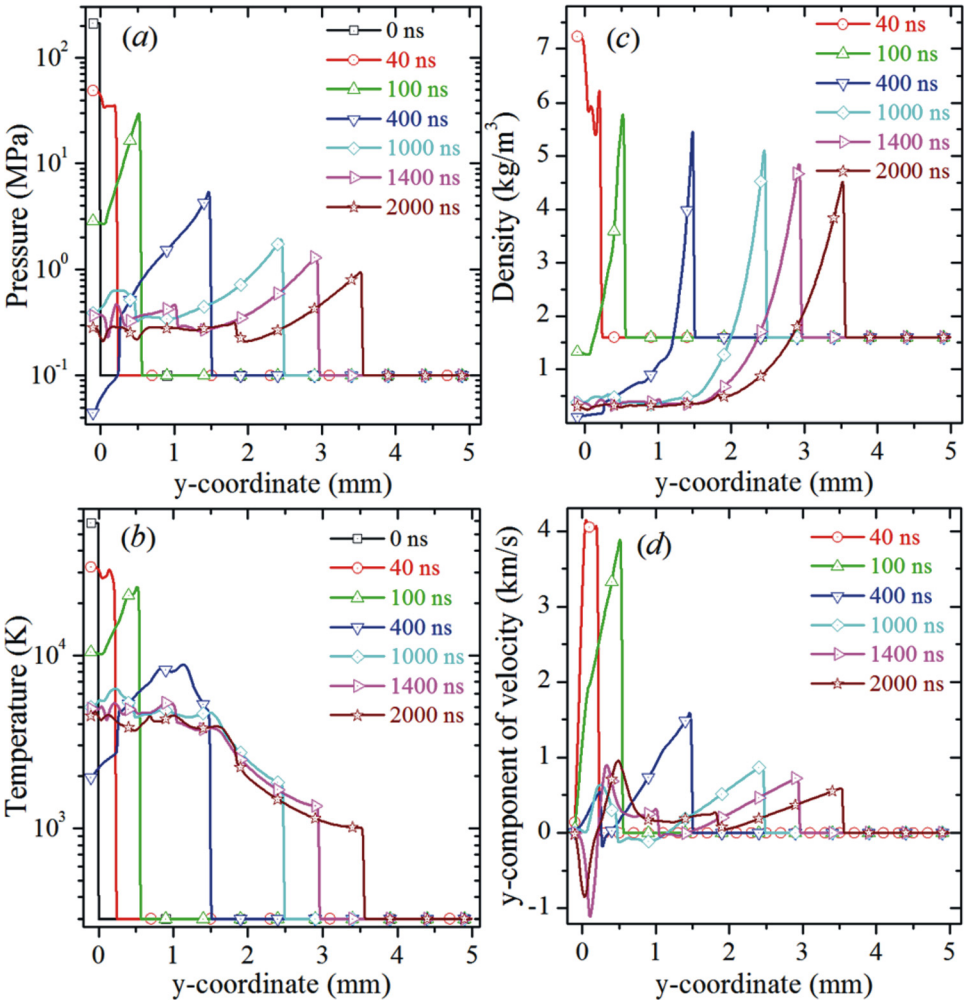

FIG. 8. Profiles of (a) pressure, (b) temperature, (c) mass density, and (d) y-component of velocity along a line perpendicular to the surface of target at the $x = 0$ for various time moments.

A contour map of pressure field is shown in Fig. 9 for different time moments. It is seen that the plasma starts to expand perpendicularly to the target surface into ambient Ar ($t \sim 100$ ns). The low-pressure region is formed in the center of plasma plume. The pressure in the normal direction is greater compared to that along the surface of the target. Due to this effect, at $t \sim 400$ ns, the nearly cylindrical column of expanding plasma develops with the pressure lower than the background Ar pressure. At $t > \sim 1000$ ns, the internal shock wave is formed close to the plume's center. The pressure increases significantly along the surface of the target. At $t \sim 2000$ ns, several oscillating shock waves are seen within the plume area. The plume transforms to a nearly symmetric shape.

The y-position of the shock front as a function of time is shown in Fig. 10 for three cases with the initial temperatures ~5, ~10, and ~15 eV. In all cases the initial pressure was kept at ~210 MPa. Therefore, the corresponding initial mass densities according to the ideal gas law are ~11.8, ~5.9, and ~3.9 kg/m^3. It is seen in Fig. 10 that during $t \sim 1000$ ns the y-position of the shock front is nearly the same. At $t > \sim 1000$ ns, the shock front of the plasma plume which exhibits a lower temperature (higher mass density) moves slightly faster. However, at $t \sim 2000$ ns, the y-location of the shock front is very close to ~3.5 mm in all three cases. These profiles of the position of shock front are in very good agreement with the experimental data (Fig. 3).

The present modeling results and the good agreement with experimental data demonstrate that the expansion dynamics of the LPP plume into an Ar atmosphere at pressure ~1 bar can be investigated using CFD modeling. The initial plasma expansion was started from an oval crater produced by the laser in the target. The plume with much higher pressure and density extrudes and pushes away the background gas. It is observed that the plasma remains close to the target surface during the early stage. The distance between the plasma front and the target surface is smaller than the size of the laser spot, and the 2-dimensional expansion of plasma is strictly normal to the surface. At later times, the cylindrically symmetric column of expanding plasma develops in agreement with our experiments (Fig. 3) and previous results.[54] Similar plasma plume dynamics was also demonstrated in studies using a one-dimensional hydrodynamic model.[27] The laser-generated plasma flow was strongly forward peaked. The dynamics of the expanding plasma changes rapidly in space and in time. At the earliest times, the asymmetric jet-like expansion is very fast and a strong shock wave is formed. However, the background gas slows down the plasma plume. At later times, the motion of plume front is significantly decelerated. The structure of the observed shock waves within the plasma plume is quite complicated. A strong shock wave moving outward and a rarefaction wave moving inward are observed initially. Then the internal shock wave arises imploding on the center of the

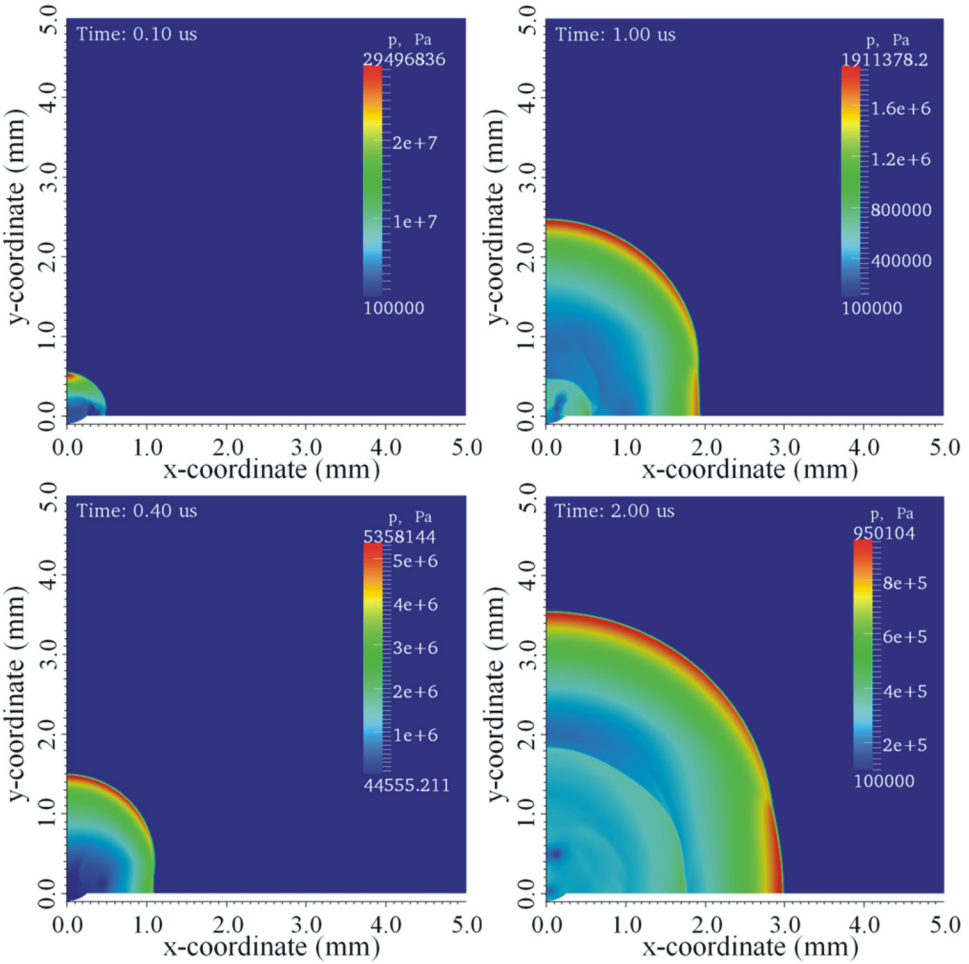

FIG. 9. Contour map of the pressure field for different time moments displayed in microseconds (enhanced online) [URL: http://dx.doi.org/10.1063/1.4745867.1].

plume at $y = 0$. It moves outward splitting at the contact boundary into the reflected and transmitted shocks. Thus, the internal shock structures in the plume develop after $t \sim 400$ ns, and this is in good agreement with our experimental observations from the fast photography (Fig. 6). The internal shock waves can travel several times between the center and front of the plasma plume. Only the early shock waves have large amplitudes and can be detected in the experiment throughout the time duration studied. The expansion with oscillating shock waves inside the plasma plume was reported in previous modeling studies.[33,36] At late times, the development of a ring-like vortex is observed in the velocity field near the surface. The vortical motion is caused by the low-pressure and low-density region formed behind the shock front.

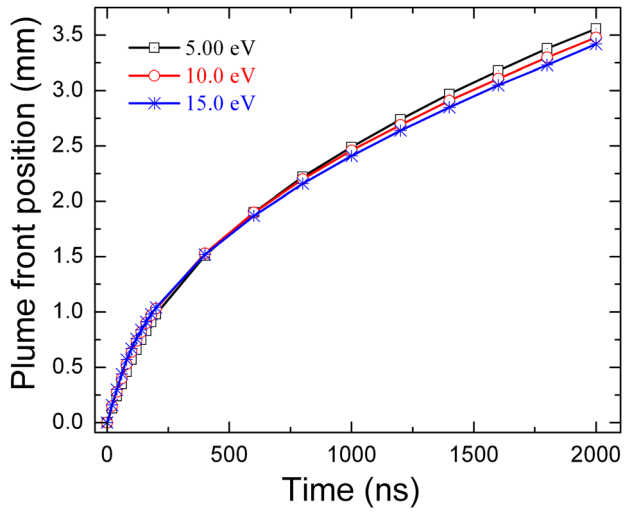

FIG. 10. The position of the front of expanding plasma as a function of time for plasma plumes with initial temperatures of 5, 10, and 15 eV.

The main focus of our computational studies is on the hydrodynamic motion of laser-produced plasma in the presence of 1 atm Ar gas. However, the plasma expansion normal to the target surface starts during the laser pulse[27] and the 3-dimensional plume propagation at the later stages is governed by the initial pressure gradients and shape of the plume at the end of the laser pulse. Our hydrodynamic model describes only the stage of plasma expansion after the end of laser pulse without treating the target heating, evaporation and ionization processes. Therefore, the pressure drops rapidly after the expansion starts. In reality, the high pressure at the surface is maintained for the duration of the laser pulse, in the present experiment the FWHM of the pulse is 6 ns, thus, significantly increasing the velocity of the plasma expansion at least by a factor of two.[20] In the present modeling, we have chosen the initial value of pressure which gives the best fit to the experimental data. The criterion was to match the position of the shock front as a function of time. The initial pressure was taken ~210 MPa. At later times the pressure is in a good agreement with the experimental estimate.

IV. CONCLUSIONS

We investigated spatio-temporal evolution of ns laser ablation plumes at atmospheric pressure, a favored condition for LIBS or LA-ICP-MS. The plasmas were generated using 1064 nm, 6 ns pulses from a Nd:YAG laser focused on an Al target. The hydrodynamics of the expanding plume in the presence of an ambient were studied using focused shadowgraphy and fast photography. Shadowgram images showed material ejection and generation of shock fronts. The shadow images recorded in the earlier times ($\leq$50 ns) showed darkened regions without any structures. This is due to high densities at early times of plasma radiation and/or spatial mixing caused by long probe laser pulse width. Internal structures inside the plume-ambient interface have been seen during the time window of 100–500 ns. A secondary shock observed behind the primary shock wave during this time window, which is also spherical through the part of the wave near to the laser cone angle, showed instabilities. The position-time plot of the secondary shock wave followed the plume front positions obtained from the self-emission and hence we concluded that the secondary shock waves are generated by fast moving target material. The instabilities noticed in the secondary shock waves at the laser cone angle are caused by laser-plasma interaction. The expansion features of plume obtained from shadowgrams were well fitted with the blast wave model.

The 2-ns gated self-emission images obtained using ICCD photography were compared with shadowgraphy images. The time sequence of ICCD images showed, similar to shadowgraphy images, rapid expansion in the first 100 ns followed by slow propagation though a distinct boundary between the plume emission zone and background was not seen. Even with 2 ns gating, the intensity features in the plume images did not show internal structures at times $\leq$250 ns. However, such internal structures are evident at later times. The plume front estimates using ICCD images showed reasonable agreement with data obtained from shadowgraphy at early times $\leq$400 ns. However, at later times ICCD images showed plume confinement while the shadowgraphic images showed propagation of the plume front even at larger times. This implies that major emission from the plasma is due to target bulk atoms/ions while the plume-ambient boundary is not generating any visible emission except the refractive changes in the medium.

Structure and dynamics of the plume obtained from optical diagnostic tools were compared to numerical simulation. We have shown that the main features of plume expansion in background argon observed in the experiments can be reproduced by the continuum hydrodynamics model. The shape of plasma plume, the pressure and position of shock front are found in good agreement with the experimental results during $t \sim 2000$ ns. The initial-stage asymmetric expansion, the internal shock-wave-like plume structure, and the vortical motion are observed. These computational results complement the experimental data providing the valuable insight into the expansion dynamics and shock structure of the plasma plume.

ACKNOWLEDGMENTS

This work is supported by the US DOE, Office of the NNSA (Award No. DE-NA0001174).

[1]J. R. Freeman, S. S. Harilal, and A. Hassanein, J. Appl. Phys. **110**, 083303 (2011).
[2]M. Crank, S. S. Harilal, S. M. Hassan, and A. Hassanein, J. Appl. Phys. **111**, 033301 (2012).
[3]S. Horne, D. Smith, M. Besen, M. Partlow, D. Stolyarov, H. Zhu, and W. Holber, Proc. SPIE **7680**, 76800L (2010).
[4]J. P. Singh and S. N. Thakur, *Laser-Induced Breakdown Spectroscopy* (Elsevier, Amsterdam, 2007).
[5]R. E. Russo, X. L. Mao, H. C. Liu, J. Gonzalez, and S. S. Mao, Talanta **57**, 425 (2002).
[6]J. O. Lay, Mass Spectrom. Rev. **20**, 172 (2001).
[7]R. Gattass and E. Mazur, Nat. Photonics **2**, 219 (2008).
[8]J. Kurian and T. Morishitaa, Europhys. Lett. **61**, 129 (2003).
[9]S. Noel and J. Hermann, Appl. Phys. Lett. **94**, 053120 (2009).
[10]P. Yeates, J. T. Costello, and E. T. Kennedy, Rev. Sci. Instrum. **81**, 043305 (2010).
[11]S. S. Harilal, T. Sizyuk, A. Hassanein, D. Campos, P. Hough, and V. Sizyuk, J. Appl. Phys. **109**, 063306 (2011).
[12]R. K. Singh and J. Narayan, Phys. Rev. B **41**, 8843 (1990).
[13]D. L. Wiggins, C. T. Raynor, and J. A. Johnson III, Phys. Plasmas **17**, 103303 (2010).
[14]A. V. Gusarov and I. Smurov, J. Phys. D **36**, 2962 (2003).
[15]A. V. Gusarov, A. G. Gnedovets, and I. Smurov, J. Appl. Phys. **88**, 4352 (2000).
[16]J. R. Ho, C. P. Grigoropoulos, and J. A. C. Humphrey, J. Appl. Phys. **78**, 4696 (1995).
[17]A. V. Bulgakov and N. M. Bulgakova, J. Phys. D **28**, 1710 (1995).
[18]M. Aden, E. Beyer, G. Herziger, and H. Kunze, J. Phys. D **25**, 57 (1992).
[19]H. L. Brode, "The blast wave in air resulting from a high temperature, high pressure sphere of air," Report No. RM-1825-AEC, Santa Monica, California, 1956.
[20]J. N. Leboeuf, K. R. Chen, J. M. Donato, D. B. Geohegan, C. L. Liu, A. A. Puretzky, and R. F. Wood, Phys. Plasmas **3**, 2203 (1996).
[21]K. F. Al-Shboul, S. S. Harilal, and A. Hassanein, Appl. Phys. Lett. **99**, 131506 (2011).
[22]S. S. Harilal, B. O'Shay, Y. Tao, and M. S. Tillack, J. Appl. Phys. **99**, 083303 (2006).
[23]S. Mahmood, R. S. Rawat, M. S. B. Darby, M. Zakaullah, S. V. Springham, T. L. Tan, and P. Lee, Phys. Plasmas **17**, 103105 (2010).
[24]S. S. Harilal, J. Appl. Phys. **103**, 123306 (2007).
[25]K. F. Al-Shboul, S. S. Harilal, and A. Hassanein, Appl. Phys. Lett. **100**, 221106 (2012).
[26]B. Rashid, R. Ahmed, R. Ali, and M. A. Baig, Phys. Plasmas **18**, 073301 (2011).
[27]M. Capitelli, A. Casavola, G. Colonna, and A. De Giacomo, Spectrochim. Acta, Part B **59**, 271 (2004).
[28]S. I. Anisimov, D. Bauerle, and B. S. Lukyanchuk, Phys. Rev. B **48**, 12076 (1993).
[29]T. E. Itina, A. A. Katassonov, W. Marine, and M. Autric, J. Appl. Phys. **83**, 6050 (1998).
[30]T. E. Itina, W. Marine, and M. Autric, J. Appl. Phys. **82**, 3536 (1997).
[31]S. Amoruso, A. Sambri, and X. Wang, Appl. Surf. Sci. **253**, 7696 (2007).
[32]S. S. Harilal, C. V. Bindhu, M. S. Tillack, F. Najmabadi, and A. C. Gaeris, J. Appl. Phys. **93**, 2380 (2003).
[33]A. V. Bulgakov and N. M. Bulgakova, J. Phys. D **31**, 693 (1998).
[34]L. I. Sedov, *Similarity and Dimensional Methods in Mechanics* (Academic, London, 1959).
[35]Y. B. Zeldovich and Y. P. Raizer, *Physics of Shock Waves and High-Temperature Hydrodynamics Phenomena* (Dover, New York, 2002).
[36]T. E. Itina, J. Hermann, P. Delaporte, and M. Sentis, Phys. Rev. E **66**, 066406 (2002).
[37]F. Garrelie, C. Champeaux, and A. Catherinot, Appl. Phys. A **69**, S55 (1999).
[38]C. J. Greenshields, H. G. Weller, L. Gasparini, and J. M. Reese, Int. J. Numer. Methods Fluids **63**, 1 (2010).
[39]OPENFOAM, The Open Source CFD toolbox, user guide, version 2.1, 2012, see http://www.openfoam.org.
[40]A. Kurganov and E. Tadmor, J. Comput. Phys. **160**, 241 (2000).
[41]H. K. Versteeg and W. Malalasekera, *An Introduction to Computational Fluid Dynamics: The Finite Volume Method* (Pearson, New York, 2007).

[42]G. Cristoforetti, S. Legnaioli, V. Palleschi, E. Tognoni, and P. A. Benedetti, Appl. Phys. A **98**, 219 (2010).
[43]M. Thiyagarajan and J. Scharer, J. Appl. Phys. **104**, 013303 (2008).
[44]J. Y. Gravel and D. Boudreau, Spectrochim. Acta, Part B **64**, 56 (2009).
[45]S. Wen, X. Mao, R. Greif, and R. E. Russo, J. Appl. Phys. **101**, 023114 (2007).
[46]G. Callies, P. Berger, and H. Hugel, J. Phys. D **28**, 794 (1995).
[47]C. R. Phipps and R. W. Dreyfus, in *Laser Ionization Mass Analysis: Chemical Analysis*, edited by A. Vertes, R. Gijbels, and F. Adams (Wiley, New York, 1993), Vol. 124, p. 369.
[48]J. Grun, J. Stamper, C. Manka, J. Resnick, R. Burris, J. Crawford, and B. H. Ripin, Phys. Rev. Lett. **66**, 2738 (1991).
[49]S. S. Harilal, M. S. Tillack, B. O'Shay, C. V. Bindhu, and F. Najmabadi, Phys. Rev. E **69**, 026413 (2004).
[50]P. Yeates and E. T. Kennedy, Phys. Plasmas **18**, 063106 (2011).
[51]W. Guan, T. Matsumoto, and T. Kawai, Chem. Phys. Lett. **291**, 161 (1998).
[52]T. P. Donaldson, J. E. Balmer, and J. A. Zimmermann, J. Phys. D **13**, 1221 (1980).
[53]K. Dzierzega, A. Mendys, S. Pellerin, E. Thouin, B. Travaille, B. Bousquet, L. Canioni, and B. Pokrzywka, J. Phys.: Conf. Ser. **227**, 012029 (2010).
[54]J. Hermann, C. Boulmer-Leborgne, and D. Hong, J. Appl. Phys. **83**, 691 (1998).